Motion Tracking Hands-Free HMI of Electric Wheelchair

Research Article

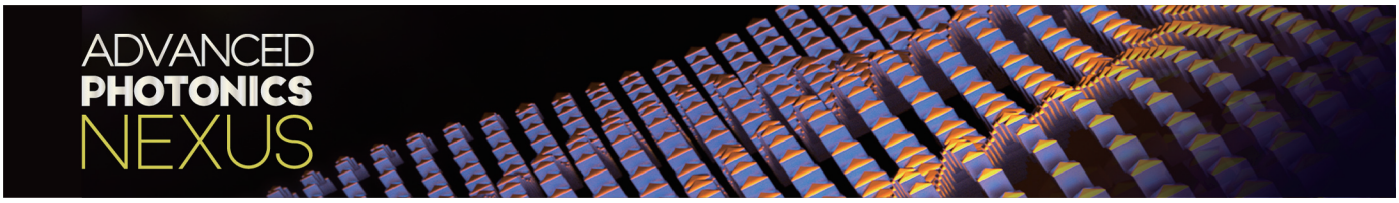

Wavevector resonance modulation in multilayered nanostructures for sub-λ/10 label-free super-resolution imaging

Haonan Zhang,[a] Xiaoyu Yang,[a,c] Mingwei Tang,[a] Conghui Gan,[a] Feihong Lin,[a,b] Emiliano Descrovi,[d] Tao Li,[e] Xu Liu,[a,b,*] and Qing Yang[a,b,f,*]

[a]Zhejiang University, College of Optical Science and Engineering, State Key Laboratory of Extreme Photonics and Instrumentation, Hangzhou, China
[b]Zhejiang University, ZJU-Hangzhou Global Scientific and Technological Innovation Center, Hangzhou, China
[c]University of Cambridge, Department of Chemical Engineering and Biotechnology, Cambridge, United Kingdom
[d]Politecnico di Torino, Dipartimento di Scienza Applicata e Tecnologia, Torino, Italy
[e]Nanjing University, College of Engineering and Applied Sciences, National Laboratory of Solid State Microstructures, Nanjing, China
[f]Shanxi University, Collaborative Innovation Center of Extreme Optics, Taiyuan, China

Abstract. Label-free super-resolution imaging based on the spatial-frequency-shift (SFS) effect enables conventional microscopes to surpass the diffraction limit, holding significant promise for nanoscale inspection in materials science and biology. However, current SFS approaches generally face a practical trade-off in obtaining both the ultra-high resolution and the high signal-to-noise ratio (SNR) when using high lateral wavevector (k_x) illumination supported by a natural waveguide or single metal film. Here, we proposed a wavevector resonance modulation scheme in multilayered nanostructures that introduces an enhanced deep SFS effect, which is realized by surface plasmon polariton illumination supported by a designed multilayer with relaxed fabrication tolerance. This approach simultaneously achieves a peak-to-peak distance of ~70 nm under the excitation wavelength of 780 nm, a resonance-enhanced illumination field, and a more than 10-fold expansion for the coherent transfer function (CTF). We demonstrated the simple excitation process by means of gratings and presented an application in nano-imaging experiments for label-free particles. Results show the advance in the resonance-enhanced illumination modulation method for super-resolution imaging, enabling conventional microscopes to detect and distinguish label-free nanoscale structures with characteristic lateral scales down to sub-λ/10.

Keywords: wavevector modulation; resonance enhancement; deep spatial-frequency-shift; super resolution imaging; label-free imaging.

Received Apr. 2, 2026; accepted for publication Apr. 28, 2026; published online May 25, 2026.

[DOI: 10.1117/1.APN.5.4.046010]

1 Introduction

Resolution of traditional microscopy is limited by the diffraction limit. The objective lens with a limited numerical aperture (NA) acts as a low-pass filter, preventing the acquisition of the high spatial frequency (SF) information of the observed sample that lies beyond the spatial cutoff frequency of the imaging system. The resolution of incoherent imaging at the scale of sub-10 nm has been achieved in previous remarkable progress through fluorescent labeling.[1–4] However, it is difficult for coherent imaging without any labeling approach to achieve ultra-high resolution. Thanks to the spatial-frequency-shift (SFS) effect,[5] the cutoff spatial high-frequency information can be shifted to the low-frequency range and transmitted to the far field, making label-free, super-resolution imaging possible through the lateral wavevector (k_x) modulation of illumination. The depth of SFS can be provided by illumination with different k_x, which is determined by the effective reflective index of the illumination space. In this framework, the lateral spatial resolution can reach

*Address all correspondence to Xu Liu, liuxu@zju.edu.cn; Qing Yang, qingyang@zju.edu.cn

up to $\lambda/(\mathrm{NA}+k_x/k_0)$, where k_0 is the wavevector in a vacuum, and the maximum NA of a commercial objective lens is 1.7 with specialized immersion oil. Thus, for the improvement of resolution, one feasible way is to increase the refractive index (n) of the illumination space to generate a higher k_x.

As for the free-space wave in air medium ($n \approx 1$), high-throughput, wide-field, and plug-and-play super-resolution imaging based on the multiangle modulation for illumination can be performed in Fourier ptychographic microscopy[6] (FPM) and related techniques[7] in this framework. Limited by the refractive index of air, the modulated k_x cannot exceed k_0, and the maximum resolution reaches a scale of about $\lambda/2$ through conventional objective lenses with NA < 1.

For deeper SFS, single nanostructures composed of layered or bulk materials with high-n have been employed to generate high-k_x illumination. The maximum k_x can be modulated to closely approach the upper limit n only by utilizing the surface localized evanescent wave produced by total internal reflection (TIR). Among the transparent materials in the visible spectrum, gallium phosphide (GaP) exhibits the highest n known to date, as we know, reaching ~3.5. Consequently, the current theoretical resolution limit for dielectric waveguide-based label-free SFS imaging is about $\lambda/4.5$.[8–12]

Surface plasmon polariton (SPP) delivered by a single metal film with nanostructures has been proven to generate higher-k_x illumination beyond the limit of dielectric materials,[13–15] based on the principle of free electron and photon oscillations. Current works have already proved that the metal film can enable a 5-time improvement in resolution[16,17] by fabricating the nanostructure array. When purposing higher resolution for label-free samples, there still exists a practical difficulty in high-k_x illumination and the demanding fabrication process for ultra-thin film,[18,19] bringing a great challenge in ultra-high resolution SFS imaging.

Above all, label-free super-resolution imaging based on SFS modulation still faces two inherent limitations when implemented using waveguides or thin films composed of a single material. First, the maximum k_x is limited only by the permittivity of the materials. Second, there exists a dilemma in obtaining high SNR illumination with high-k_x, due to the unavoidable sacrifice in photon intensity of a highly surface localized illumination field.[20,21] Thus, the SFS modulation for generating illumination with both field enhancement and high-k_x is critical to ultra-high resolution label-free imaging.

The resonance effect brought by multilayered structures has been widely utilized in frequency mode selection[22,23] and field enhancement.[24,25] To alleviate the conventional trade-off and realize ultra-high resolution for label-free imaging, it is desired to develop a resonance modulation method in the spatial frequency domain that can bring more abundant modulations for generating enhanced high-k_x mode for deep SFS.[26] By contrast, a more fundamental question remains insufficiently explored: whether the spatial-frequency response itself can be actively engineered to selectively enhance desired high-wavevector channels for imaging. Addressing this question would move SFS imaging beyond material selection alone and toward a more general framework of resonance design in wavevector space.

In this work, we introduced wavevector resonance modulation in designed multilayered nanostructures for sub-$\lambda/10$ label-free super-resolution imaging based on the enhanced deep spatial-frequency-shift (EDSFS) effect. The multilayered nanostructures mainly provide three advantages. First, the multilayer builds the spatial frequency-enhanced cavity and supports SPP with k_x exceeding $10k_0$, while strongly amplifying its intensity. Second, it enables detection enhancement of wavevectors in a broad spatial range in one illumination process at a single wavelength under multiple resonant wavevectors. Lastly, our design for multilayer can provide relaxed fabrication constraints of multilayer with over 10 nm thickness of metal layer and maximum 4 nm thickness error tolerance through purposely designed tailoring for wavevector modulation. The results prove that EDSFS by multilayer can enable an NA-limited microscope to detect label-free samples, including slot pairs and nanoparticles, at the scale of sub-$\lambda/10$ with multiple and ultra-high spatial frequency components.

2 Results

2.1 Theory Analysis of EDSFS Effect Brought by Resonance MIM Multilayer Structure

As for the generation of SFS illumination for super-resolution imaging through wavevector modulation, we use the metal–insulator–metal (MIM) multilayer structure to excite the SPP mode as illumination with TM polarization, and it is integrated with the microscope [Fig. 1(a)]. In this way, the surface wave propagating along the interface at the top metal layer and imaging area (air) can be efficiently coupled in conditions of wave vector matching. The maximum k_x of the illumination field depends on the dielectric constant of the metal and insulator materials, as well as the thickness of the metal and insulator film that constitutes the multilayer structure. Generally, we introduce a purposefully designed MIM multilayer that supports SPP with maximum k_x, which can be 10-fold more than the wavevector in vacuum k_0.

In addition, 4 nm thickness error tolerance of each layer can be permitted while remaining fully compatible with simple, scalable deposition processes [Fig. 1(b)] (see Note S1.1 in the Supplementary Material for more detailed discussion about the principle of the design process). Compared with ultra-thin single metal films, our method delivers a fabrication-friendly platform. In contrast, high-k_x modes supported by single-layer metal films require both plane nanostructures fabricated and a thickness of sub-10 nm, bringing high precision for fabrication.

We fabricated the MIM multilayer with 44 nm-Au, 7.3 nm-TiO_2, and 12.8 nm-Au (see Fig. S6 in the Supplementary Material for detailed fabrication process), with a cross-section image obtained by a transmission electron microscope (TEM) [Fig. 1(c)]. Notably, the MIM multilayer structure builds a Fabry–Pérot cavity, which means it can support the enhanced selected illumination mode with high-k_x propagating at the interface owing to the resonance effect. In fact, in real space, an enhanced intensity can be observed associated with the surface modes supported by the multilayer, as shown in the inset of Fig. 1(c). Field intensity at the MIM surface is calculated as an analytical solution for E_x (see Note S1.2 in the Supplementary Material). Alternatively, the electric field distribution through the multilayer can be calculated as shown in the simulation result [Fig. 1(d)]. In the k-space, the phase delays introduced by the transmission and reflection coefficients at each interface influence the resonance condition, leading to mixed and enhanced wavevector components. The whole phase delay can be denoted as the following equation: $\phi = k_z d_{\mathrm{TiO_2}} + \varphi_{\mathrm{in}} + \varphi_{\mathrm{out}}$, where φ_{in} and φ_{out} result from the reflections at the bottom

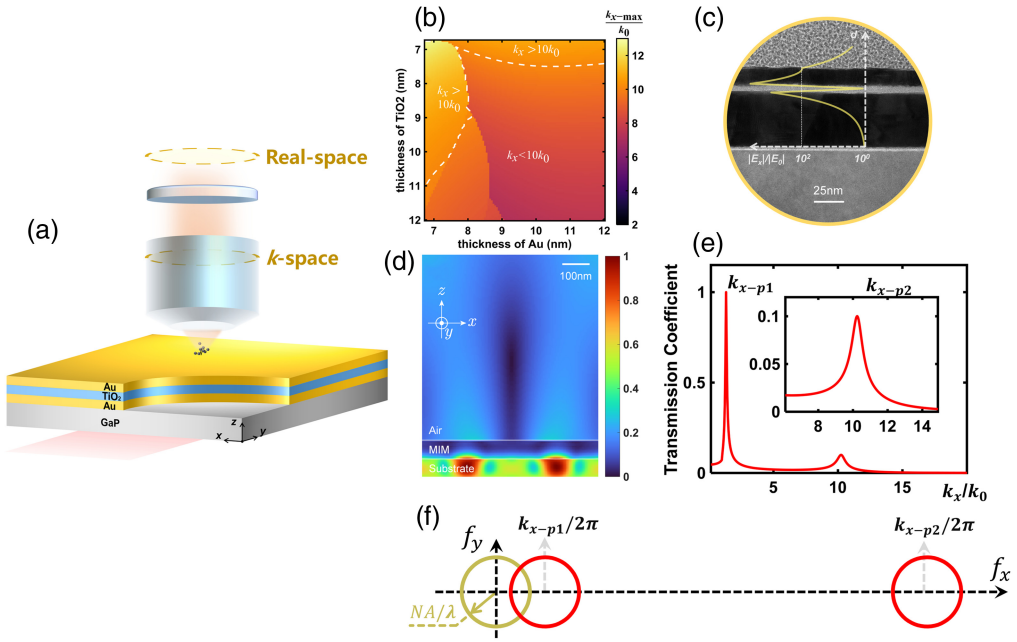

Fig. 1 Super-resolution chip based on the EDSFS effect. (a) The schematic of the MIM structure and EDSFS effect detected in real-space and *k*-space. (b) The maximum k_x supported by multilayer varies with different thicknesses of each layer. (c) The TEM image of the multilayer cross-section and the theoretical enhanced electric field curve in the *x*-axis of each layer under TM polarization. (d) Simulation of the electric field distribution in the *xz*-plane when the incident light travels through the chip. (e) The resonant-enhanced wavevectors supported by the EDSFS super-resolution chip. (f) The schematic of the range of EDSFS.

and top of Au layers, i.e., $\varphi_{in} = \arg[(n_{sub} - k_z/k_0)/(n_{sub} + k_z/k_0)]$ and $\varphi_{out} = \arg[(k_z/k_0 - n_{air})/(k_z/k_0 - n_{air})]$, respectively.[27] Especially when $\phi = 2m\pi$ (the integer m indicates the number of the enhanced modes), several modes can be excited at different transverse wavevectors, which then propagate at the top layer of the MIM structure, eventually contributing to the enhanced spatial-frequency components in the *k*-space. From another perspective, to analyze how wavevectors are modulated, we calculate the transmittance coefficient of each lateral wavevector component supported by the multilayer through the transfer-matrix method (TMM; see Note S1.3 in the Supplementary Material) and plot the value of the transmittance coefficient of different lateral wavevectors in Fig. 1(e), which shows that the two resonance points of all components exist at the same time ($k_{x\text{-}p1} = 1.15k_0$, $k_{x\text{-}p2} = 10.18k_0$). Furthermore, the two enhanced wavevector components in the spatial frequency domain and the enhanced near-field illumination in the spatial domain contribute to EDSFS as a result of the resonant effect; part of the spatial frequencies of the sample contained within the scattering light can be shifted within the cutoff frequency range of the NA-limited objective lens in EDSFS. The range of spatial frequency of objects detected by the objective lens with NA = 0.8 in an EDSFS configuration is shown in Fig. 1(f). Although the present proof of concept uses Au and TiO_2 at 780 nm, the EDSFS mechanism is not limited to this specific material-wavelength combination. It can be extended to other wavelengths and other material combinations. The supported resonance k_x components can, in principle, be reconfigured by jointly tuning the dielectric functions, layer thicknesses, and excitation wavelengths of the multilayer platform. In this experiment, we detected the SFS effect caused by mixed wavevector modulation through the MIM structure in both real-space (directly imaging for the sample) and *k*-space (imaging for the spatial frequency of the objective lens). The real space for SFS images expresses the super-resolution performance, and *k*-space for the back focus plane (BFP) of the objective lens shows the spatial frequency range of objects detected by the system directly. Through dual-space detection, the EDSFS effect brought by the multilayer system we proposed can be clearly illustrated.

2.2 EDSFS Excitation for Super Resolution Imaging

The super-resolution imaging process based on EDSFS relies on the critical factor, namely the excitation of high-k_x modes at the top-layer interface, aimed at illuminating the sample for ultra-high resolution imaging. To satisfy the wavevector matching condition, we etched a grating with a sub-$\lambda/10$ period (71 nm) by means of a focused ion beam (FIB) micro-nano processing system (Carl Zeiss, Quanta 3D FEG). It is worth emphasizing that we etch through the whole multilayer (the depth of etching is set as 140 nm). The GaP substrate is then etched with the same period of the grating to avoid the adhesion layer (Cr) obstructing the excitation process. On the other hand, the gratings can be used to excite the high-k_x illumination. Conversely, the grating's rough edges promote scattering when illuminated by the high-k_x mode. Furthermore, on the condition that the spatial frequency of the object is the Fourier transform of the sample, we can regard structures as the combination of nano-gratings with mixed spatial frequencies. The image of the rough edges of the grating and the scanning electron microscope (SEM) image of the representative etched slot-pair region as

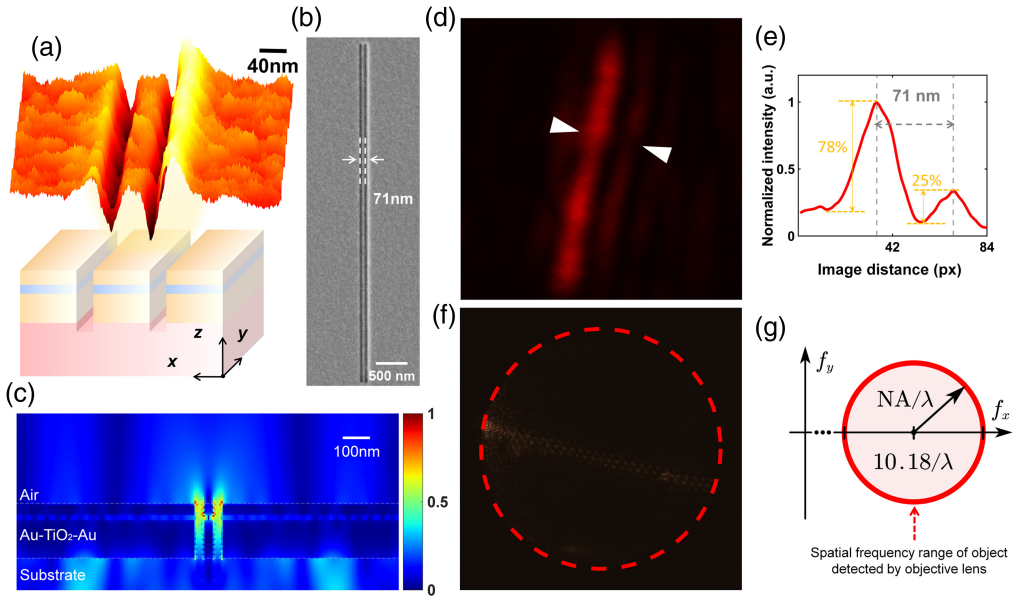

Fig. 2 Illustration of EDSFS for super-resolution imaging through grating illumination. (a) The image of the rough edge of the grating measured by the SEM (upper) and the schematic of the grating etched through the multilayer (lower). (b) SEM image of the representative etched slot-pair region. (c) Simulated distribution of the electric field across a vertical cross-section of the structure. (d) Super-resolution image of the slot pair in real space. (e) The intensity profile of the imaged structure arrowed in (d). (f) BFP image of the objective lens in *k*-space. (g) Schematic of the spatial frequency range detected in (f).

seen by the SEM (Carl Zeiss, Ultra 55) are shown in Figs. 2(a) and 2(b), respectively. When the resonance-enhanced high-k_x illumination is excited by TM-polarized light, it can interact with the edges of the grating and result in scattering. Under the condition of wavevector matching, the corresponding vertical electric field distribution in a vertical cross-section is shown in Fig. 2(c). Scattered light propagating in air is related to the real-wavevector space and carries high spatial frequency information about the object. As it travels to the far-field, it can be collected within the objective NA. In the spatial domain, the slot pair with the period of 71 nm can then be distinguished in the real-space [Fig. 2(d)]. The corresponding intensity profile with center-to-center distance is plotted in Fig. 2(e). The observed intensity asymmetry between adjacent slots is primarily attributed to fabrication-induced variations in etch depth and edge roughness, rather than an intrinsic asymmetry of the EDSFS imaging mechanism (see Fig. S8 and Note 4 in the Supplementary Material). In the frequency domain, the center of the frequency passband of the objective lens is shifted from the origin point (0, 0) of the f_x-axis and the f_y-axis (the center frequency in diffraction-limited imaging, i.e., the optical frequency axis) to the point $(10.18/\lambda, 0)$ that represents the maximum center frequency in EDSFS. The BFP image recorded by the *k*-space detector shows the spatial frequency of the slot pair detected by a 0.8 NA objective lens under the illumination provided by the 71 nm period grating [Fig. 2(f)]. The schematic of the spatial frequency range is shown in Fig. 2(g). To further illustrate the effectiveness of the EDSFS method to provide super-resolution imaging under large spatial frequency loss, the center-to-center distance in Fig. 2(e) is 31 px of image distance. Due to the spatial frequency loss under the high-k_x illumination, the real-space images of the resolved sub-$\lambda/10$ samples exhibit distortions originating from both the optical magnification of the optical system and the EDSFS magnification caused by deep SFS (see Note 2 in the Supplementary Material for further details). Here, we use a real-space detector with a 6.5 μm pixel size and an optical magnification of about 200× (100× magnification of objective lens, 2× magnification of beam expansion before detector). The real size (71 nm) of the period of the slot pair was measured by an SEM, and the pixel distance (31 px) was measured in the raw image. The experimental pixel distance nearly matched the theoretical result (see Table S1 in the Supplementary Material). The error of 1 px may originate from the experimental optical magnification. In short, we employed EDSFS for super-resolution imaging through grating and successfully shifted the passband of the objective lens to the range of high spatial frequency of the object [Fig. 2(f)].

In the real-space image, we observe that the sub-$\lambda/10$ slot pair can be clearly distinguished under a modulated illumination, with $k_x = 10.18k_0$. Conversely, from the *k*-space image, our EDSFS method shows a great performance in collecting high-frequency scattered light ($k_x/k_0 > 12\,\mathrm{NA}$), leading to ultra-high resolution of label-free optical microscopy imaging, as expressed in the following equation $r = \lambda/(\mathrm{NA} + k_x/k_0) < \lambda/13\,\mathrm{NA}$. Notably, when a smaller NA of the objective lens is used, the relative improvement of imaging resolution will be beyond $\lambda/13\,\mathrm{NA}$ (such as $\lambda/102.8\,\mathrm{NA@NA} = 0.1$ in theory). We show the simulated SFS images by objective lenses with different NAs in Supplementary Note 2 (see Fig. S3 in the Supplementary Material). In conclusion, the structure of the $\lambda/10$ period can be distinguished objectively from the various NAs.

2.3 EDSFS Imaging for V-shaped Slot Structure

Due to the resonance effect, illumination with two enhanced wavevector modes can be excited simultaneously. To directly show the mixed wavevector modulation brought by the resonance effect, we fabricated a grating with a continuously varying period from ~70 to ~700 nm to excite the whole wavevector components supported by the multilayer. The grating possesses continuous spatial frequency components from $\sim 1/\lambda$ to over $\sim 10/\lambda$, which shows a V-shaped slot pair shape. Here, we etched the grating by FIB and used near circular polarized light for excitation, which we recall including both the MIM structure and the GaP substrate. In this configuration, the TM-polarized component can excite the high-k_x SPP mode supported by the MIM structure ($k_{x\text{-}p1} = 1.15k_0$ and $k_{x\text{-}p2} = 10.18k_0$) whilst the TE-polarized component can excite another mode supported by the substrate ($k_{x\text{-TE}} = 2.37k_0$, according to effective medium theory[28]), as shown in Fig. S3 in the Supplementary Material.

Hence, we can obtain the mixed modulated wavevector through the multilayer system by the circular polarization exciting [Fig. 3(a)], leading to three main k_x components. Thus, the relevant imaging resolutions obtained with an NA = 0.8 objective lens at the wavelength of 780 nm due to the mixed wavevector modulation can be ~400 nm@$k_{x\text{-}p1} = 1.15k_0$, ~245 nm@$k_{x\text{-TE}} = 2.37k_0$, and ~72 nm@$k_{x\text{-}p2} = 10.18k_0$, respectively. In the frequency domain, the mixed wavevectors supported by the multilayer system enable three different SFS depths. This allows the spatial frequency components of the sample located at $(1.15/\lambda, 0)$, $(2.37/\lambda, 0)$, and $(10.18/\lambda, 0)$ to be shifted within the frequency passband of the objective lens

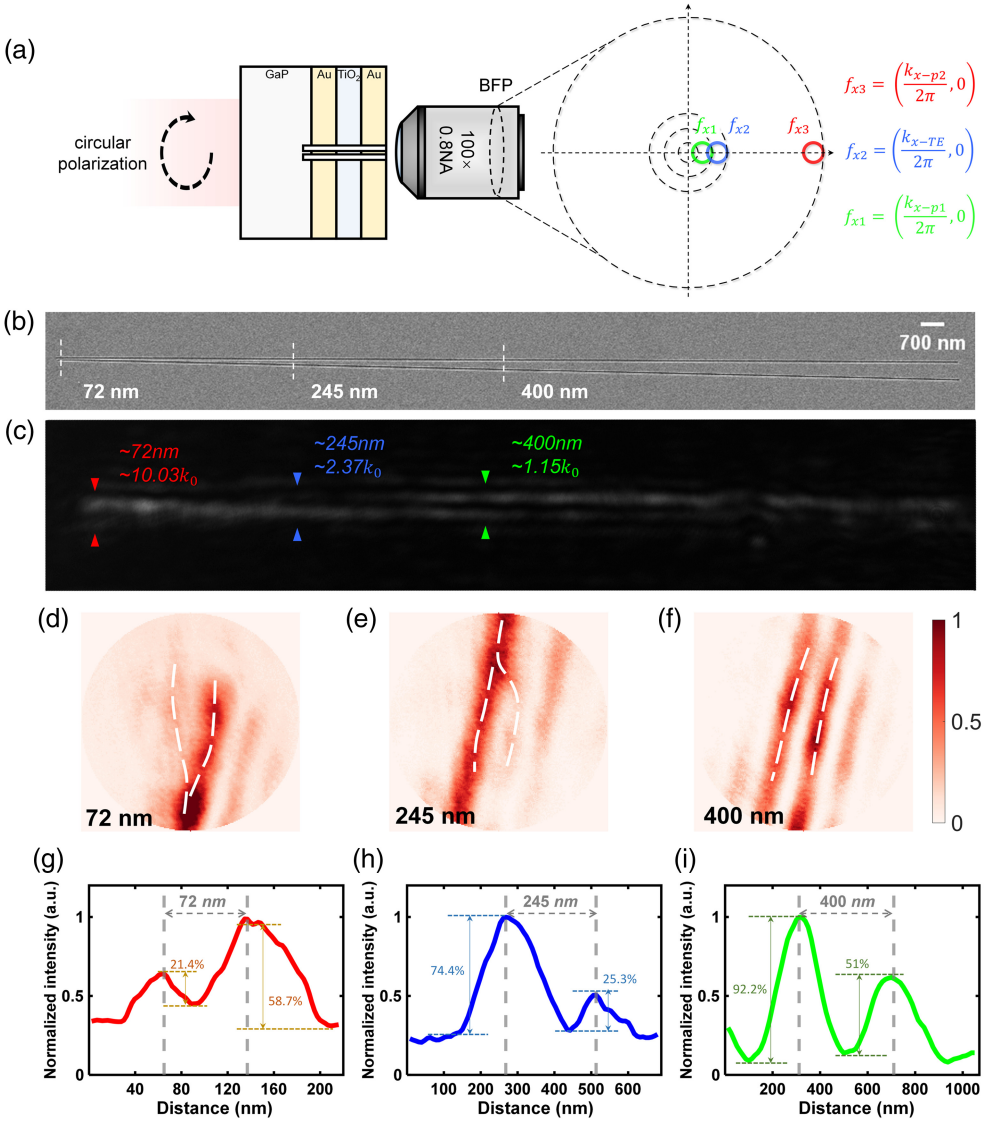

Fig. 3 Mixed wavevector modulation in EDSFS based on the multilayer system. (a) The schematic of the mixed wavevector illumination process. (b) The SEM image of the V-shaped slot pair. (c) The original image of the V-shaped slot pair under the illumination with the mixed wavevector in the experiment. Panels (d)–(f) show the zoomed-in views corresponding to the three analyzed positions. Panels (g)–(i) show the intensity profiles of the three period positions corresponding to the three wavevectors.

simultaneously in just one illumination process. In the schematic of mixed SFS, the above spatial frequency ranges collected by the objective lens are respectively marked by green, blue, and red circles in Fig. 3(a).

An SEM image of the V-shaped slot pair is shown in Fig. 3(b), and the approximate positions of the relative distance in illustrative points are marked by dashed lines. When the illumination field with circular polarization is incident on the multilayer, the three main periods of the V-shaped grating can be distinguished at the same time [Fig. 3(c)] because the different enhanced wavevectors must be excited under the specific conditions of wavevector matching through different period structures. In other words, the three structures are primarily discriminated by their distinct wavevector-matching conditions rather than by computational separation. Therefore, each resonant channel predominantly probes sample features whose local spatial frequencies fall within its effective coupling window. Although partial overlap may exist in practice, the large separation between the supported resonant wavevectors and the selective resonance enhancement suppresses substantial mode mixing in the present experiment. The corresponding zoomed-in views and intensity profiles of these three positions, arrowed in Fig. 3(c), are shown in Figs. 3(d)–3(f) and Figs. 3(g)–3(i), while the image distances also nearly match the theoretical results (Table S1 in the Supplementary Material). To further illustrate the illumination with mixed modulated wavevectors for super resolution imaging, we use another microscope with a real-space detector with a 5.5 μm pixel size and an optical system with 100× optical magnification. The results are consistent with the theoretical expectations (Fig. S8 in the Supplementary Material). We show the Fourier transform of the SEM images and the SFS images (Fig. S9 in the Supplementary Material), which corresponds to the two enhanced wavevectors supported by the MIM structure.

2.4 EDSFS for Label-free Sub-$\lambda/10$ Nano Imaging of PMMA Particles

To illustrate the enhanced near-field illumination credibly, we choose PMMA, the dielectric particles with a relatively low reflective index, as the imaging sample. It also proves the multilayer system can support illumination through high lateral wavevector ($k_x > 10k_0$) waves propagating at the MIM interface. Here, we use the high-k_x waves to illuminate the nanodielectric particles $30-40$ nm in size. We drop-cast PMMA particles ($n = 1.4847@\lambda = 780$ nm) onto the top surface (Au) of the multilayer, then etch the excitation grating next to the particles to ensure that some nanoparticles can be reached within the SPP propagation distance from the grating. The use of low-index dielectric PMMA nanoparticles, therefore, provides a more stringent test of the EDSFS mechanism than plasmonic resonant metallic particles. When a TM-polarized wave is incident onto the MIM structure, the SPP mode can be coupled so that it can illuminate the particles, resulting in scattering. Notably, the reason why we choose dielectric particles instead of metal particles is that it is necessary to avoid the other influence from localized resonance brought by metal particles.

The results indicate that dielectric nanoparticles with characteristic diameters of ∼30 to 40 nm can be optically detected and distinguished when their separations approach ∼70 to 100 nm under EDSFS illumination. Original images of different regions of interest (ROIs) are in Figs. 4(a) and 4(e). ROI1 and ROI2, framed by the blue and orange squares, show that particles with different separation distances can be distinguished. The corresponding ground truth images obtained by the SEM are shown in Figs. 4(b) and 4(f), and the SFS images of the particles framed in Fig. 4(a) (with lateral periods of 98 and 73 nm, as measured by the SEM) and those in Fig. 4(f) (with a lateral period of 71.2 nm) are enlarged and presented in Figs. 4(c) and 4(g), respectively. The corresponding intensity profiles of ROI1 and ROI2 marked by arrows are plotted in Figs. 4(d) and 4(h). This experiment demonstrates the detectability and distinguishability of weakly scattering dielectric nano-objects, rather than a direct one-to-one measurement of isolated particle diameter.

From the collected SFS images related to nanoparticles with different separation distances along the direction of the excitation gratings, we can see that particles in the $30-40$ nm diameter range with separations from ∼70 to ∼100 nm can all be distinguished but in different image distances, which also proves that the continuous wavevector modulation brought by the MIM structure can lead to a wide frequency range in the coherent transfer function (CTF) of the objective lens with a 0.8 NA at the wavelength of 780 nm, due to more than one enhanced lateral wavevectors, which means mixed wavevectors. We show the CTF under different illumination modes and compare the CTF in our method with other SFS methods in Note S6.3 in the Supplementary Material. A wider CTF range can be modulated at a single wavelength of 780 nm and a single excitation in EDSFS. Analyzed from the results shown in Fig. 4, the minimum effective modulation range of k_x is $[8.6k_0, 10.15k_0]$, which proves the ability of our method to enhance the CTF of a traditional microscope to a wide and deep spatial frequency. Moreover, by designing a multilayer capable of generating even higher k_x, our approach holds promise for enabling the observation of sub-30 nm periodic structures. We show the designation for over $20k_0$ at an excitation wavelength of 638 nm in Fig. S2 in the Supplementary Material.

3 Discussion and Conclusion

In this work, we demonstrated that an enhanced optical field associated with a specific lateral wavevector can be generated through resonance modulation supported by an MIM structure and can be used as an enhanced near-field illumination for deep SFS label-free super-resolution imaging. The proposed approach is compatible with traditional microscope configurations to implement ultra-high imaging resolution. We provided exemplary raw super-resolution images of dielectric objects under surface-localized illumination fields with a high SNR under deep SFS illumination ($k_x/2\pi \gg 2\,\mathrm{NA}/\lambda$). Compared with previous SFS modulation, the resonance modulation in the lateral wavevector leads to great signal enhancement under near-field illumination with an ultra-high spatial frequency. As shown in Fig. 5, for natural waveguides, the maximum k_x cannot exceed $3.5k_0$, which is limited by the refractive index, the intensity of illumination is limited by the scattering light that exits in a large incident angle ($E_{\mathrm{illu}} \propto E_0 \cos\theta$) or total internal reflection ($E_{\mathrm{illu}} \propto E_0 \exp[-k_0\sqrt{(n\sin\theta)^2 - n_0^2}]$ in each nanostructure and the coherent scattering $\mathbf{S}(\mathrm{K})$ all contribute to the enhanced intensity ($E_{\mathrm{illu}} \propto E_0 \cdot \alpha(\lambda)/(1\text{-}\alpha(\lambda)\mathbf{S}(\mathrm{K}))$. We designed a multilayer structure that can significantly enhance the SNR of illumination with deep SFS, where the maximum k_x of illumination can be enhanced by the resonance effect. Besides the oscillations of electrons and photons, the multilayer, in addition to

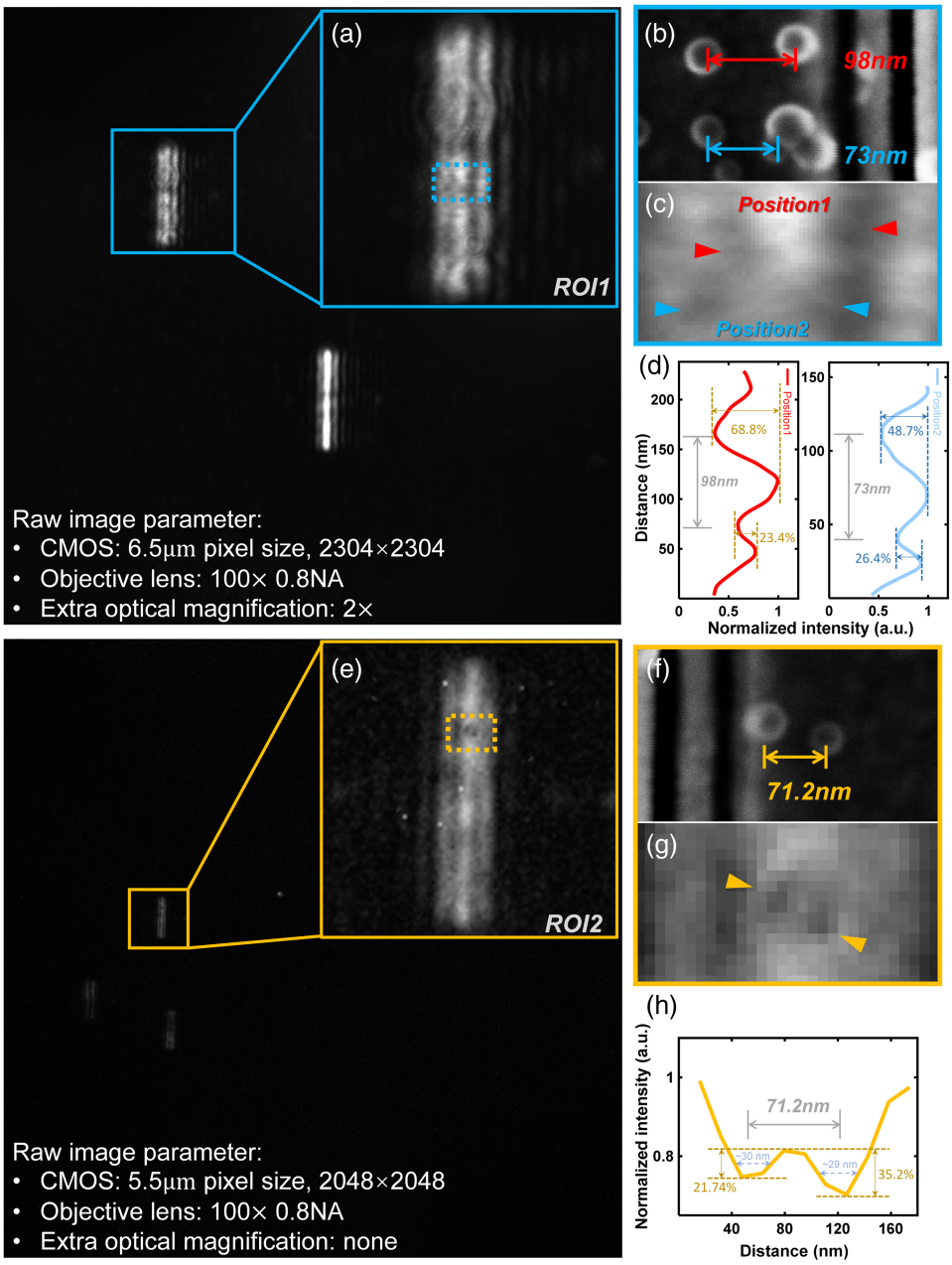

Fig. 4 EDSFS for label-free super-resolution imaging of nanoparticles within a wide frequency range in the experiment. (a) Raw SFS image of ROI1 obtained by system 1. Panels (b)–(d) show the SEM image, enlarged SFS image, and intensity profiles corresponding to ROI1. (e) Raw SFS image of ROI2 obtained by system 2. Panels (f)–(h) show the SEM image, enlarged SFS image, and intensity profile corresponding to ROI2.

its field enhancement capability, and the cavity, composed of the multilayer, also exhibit a resonance enhancement specifically for the spatial-frequency mode of the transmission wave.

In short, EDSFS by multilayer provides a mixed wavevector resonance modulation method to perform a 2-time enhanced near-field-illumination (enhancement in illumination intensity compared with other surface waves; see Note S6.1 in the Supplementary Material), 3-time SFS-deepened compared with natural waveguides (leading to over $10/\lambda$ shift in the frequency domain), and large-range CTF-widened (mixed-wavevector generation under coherent excitation; see Note S6.2 in the Supplementary Material), which endows traditional microscopes with ultra-high resolution capabilities without any complex sample preparation and special fluorescent labeling. EDSFS makes it possible to realize ultra-high optical imaging resolution for label-free samples through a simple imaging slide (see Note S6.3 in the Supplementary Material), leading to more possible applications in nano-particles detection, biological, and chemical research.

From a practical standpoint, several implementation-related factors also influence the current proof-of-concept performance. Fabrication imperfections in the coupling grating, such as edge

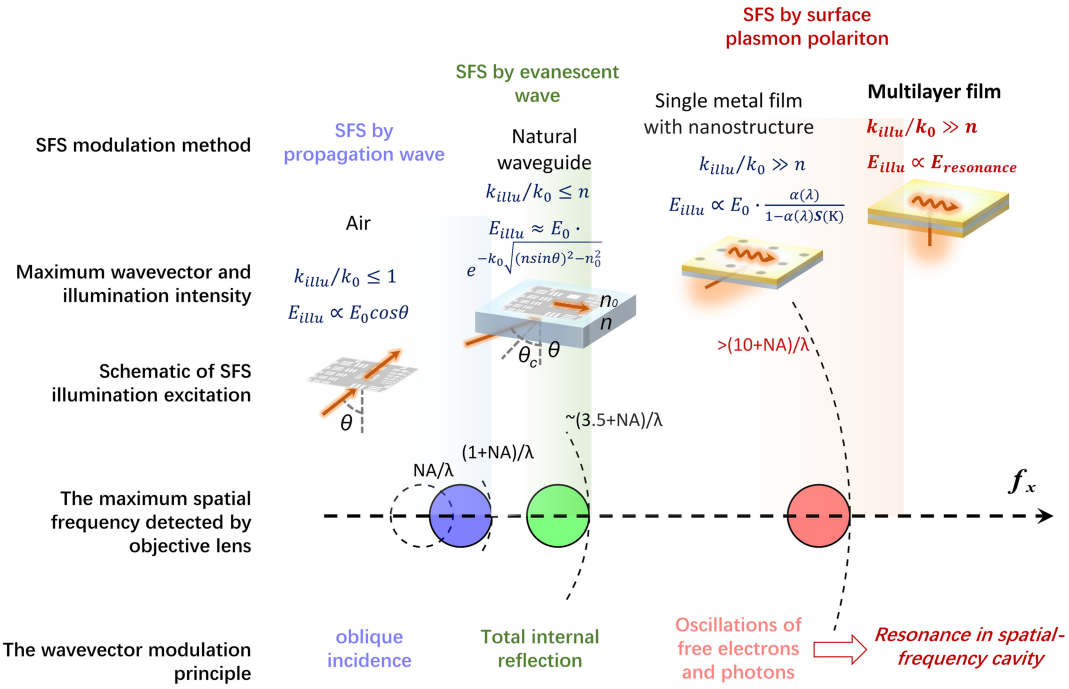

Fig. 5 Principle, techniques, and performance of different SFS modulation methods.

roughness, local period variation, and duty-cycle deviation, can affect the coupling efficiency and illumination uniformity of the launched surface waves. However, these imperfections primarily influence signal strength and spatial uniformity, rather than invalidating the EDSFS mechanism itself. Future implementations may address this limitation through distributed coupling structures, larger-area excitation designs, or more scalable integrated illumination geometries.

4 Appendix: Methods

4.1 MIM Structure Design for Wavevector Modulation

In this work, we designed and fabricated the MIM structure to generate the SPP wave. We calculate the maximum lateral wavevector ($k_{x\text{-max}}$) supported by the MIM structure through Maxwell's equations of the electromagnetic field and the boundary condition. Then, we can solve the $k_{x\text{-max}}$ through the five optimization equations, as well as the intensity of the electric field at the interface between the top layer and air [see Fig. 1(b) and Fig. S11 in the Supplementary Material]. The detailed expressions and more calculation results are shown in Note 1 in the Supplementary Material. Aiming to make the multilayer system compatible with more samples, we chose Au as the metal material, which is chemically stable in air or water. To generate a higher lateral wavevector, we chose TiO_2 as the insulator material. Finally, we designed the MIM structure with 44 nm-Au, 7.3 nm-TiO_2, and 12.8 nm-Au, which was fabricated by the physical vapor deposition (PVD) and atomic layer deposition (ALD) processes. The detailed process of the multilayer and the sample preparation are shown in Note 3 in the Supplementary Material. Besides, we analyzed and calculated the transmission coefficient of the light with the whole lateral wavevector when traveling through the multilayer by traditional TMM in theory, shown in Fig. 1(d). Finally, we can excite the two individual enhanced lateral wavevector components in the procedure of wavevector matching. Although the present experimental implementation uses an Au/TiO_2-based multilayer operating at 780 nm, the EDSFS design principle is not restricted to this specific material–wavelength combination and can be re-optimized for other wavelengths and material systems, as discussed in Note 1 in the Supplementary Material.

4.2 EDSFS Effect in Both Spatial Domain and Frequency Domain

For the basic situation that all the fine structures of the object can be regarded as the combination of the grating-shaped structures with different periods, we analyze the general case that the spatial frequency of the grating-shaped object with the lateral period of d and each line width of l can be expressed as $f_{\text{obj}} = \vec{C} \cdot \cos(\pi d \cdot f_x) \cdot \text{sinc}(l \cdot f_x)$.[5] The frequency component related to the period is the cosine function, which means that the standard of the distinguished structures in the frequency domain is that at least two orders of the spatial frequency of the object can be collected by the objective lens. Here, for the EDSFS we proposed, the basis for judging the correct super resolution is the enlarged image distance, which is affected by the combination of the SFS magnification and the optical magnification illustrated above in the spatial domain, which leads to the distortion for the real size of the object. In the frequency domain, we use a 4*f*-pair to image the BFP of the objective lens, which contains the information of the first Fourier transform of the object. A continuous, periodically changing intensity distribution expresses the least two orders of the object collected by the objective lens (see Fig. S5 in the Supplementary Material). In this work, we show the images in the spatial domain and the frequency domain experimentally, shown in Figs. 2(d) and 2(f). In addition, in Fig. 2(f), the intensity shows one more

periodic variation because the gratings with different periods are all in the field of view (FOV) of the objective lens.

4.3 Imaging System Setup

We set up two microscope systems in this work; the difference between the two lies in the optical magnification and the real-space detector to prove the EDSFS performance for super-resolution imaging sufficiently (Notes 3 and 4 in the Supplementary Material). First, we showed the same parts in the two systems. The laser emitted by a 780 nm laser diode (LBTEK, LM32-780-C) travels through the collimating lenses and its polarization is modulated by the polarizer, and wave plates of $\lambda/2$ and $\lambda/4$ to the linear polarization (TM) and circular polarization. The experimental results in Figs. 2(d), 2(f), 4(a), 4(c), 4(e), and 4(g), as well as Figs. S8(a) and S8(c) in the Supplementary Material, were under the excitation condition of TM polarization. The experimental result in Fig. 3(c) was under the excitation condition of circular polarization. The detailed schematic of the optical path is shown in Fig. S6(a) in the Supplementary Material. Then, we use the objective lens (OLYMPUS, LMPlanFLN 100× 0.8 NA) to collect the scattering light, which travels through the tube lens (LBTEK, ITL200-B). The scattered light is divided by two paths, one travels to the plane of the real-space detector, and the other travels through an imaging lens ($F = 400$ mm) to the plane of the k-space detector (JCOPTIX, AIC-502M-USB), where we obtained the results shown in Fig. 2(f). In one system, we set a telescope with 2× magnification (containing two lenses: $F1 = -30$ mm, $F2 = 60$ mm) before the real-space detector (Hamamatsu, ORCA-Fusion C14440-20UP), where we obtained the results shown in Figs. 2(d), 3(c), 4(a), and 4(c). In the other, we only set the real-space detector (JCOPTIX, AIC-401GC-USB) without a telescope, where we obtained the results shown in Figs. 4(e) and 4(g), as well as Figs. S8(a) and S8(c) in the Supplementary Material. A concise comparison of the two microscope configurations is summarized in Table S1 in the Supplementary Material.

4.4 Simulation Method and Platform

The following simulation or calculation results were implemented in MATLAB software: the results in Fig. 1(b) and Fig. S1 in the Supplementary Material were obtained by the gradient descent solution algorithm; the result in Fig. 1(d) was obtained by the TMM; the results in Figs. 1(e) and 3(a), as well as Figs. S1, S4, S5, S12, and S13 in the Supplementary Material, were obtained by home-built algorithms. Moreover, the simulation results in Figs. 1(c) and 2(c), as well as Fig. S11 in the Supplementary Material, were implemented using FDTD simulation.

Disclosures

The authors declare no competing interests.

Code and Data Availability

All data needed to evaluate the conclusions in the paper are present in the paper and/or the Supplementary Material.

Acknowledgments

This work was supported by the National Natural Science Foundation of China (Grant Nos. T2525010, T2293751, and 2024YFF1206700) and the Leading Innovative and Entrepreneur Team Introduction Program of Zhejiang (Grant No. 2024R01001). The authors sincerely thank Wei Wang at the State Key Laboratory of Extreme Photonics and Instrumentation, Zhejiang University, for her great assistance with FIB and SEM. The authors also thank Yongchen Ji (currently a PhD student of Zhejiang University) for his help with spin-coating PMMA particles.

References

1. D. A. Helmerich et al., "Photoswitching fingerprint analysis bypasses the 10-nm resolution barrier," *Nat. Methods* **19**, 986–994 (2022).
2. Y. Han et al., "Three-dimensional multi-color optical nanoscopy at sub-10-nm resolution based on small-molecule organic probes," *Cell Rep. Methods* **3**, 100556 (2023).
3. M. Dai, R. Jungmann, and P. Yin, "Optical imaging of individual biomolecules in densely packed clusters," *Nat. Nanotechnol.* **11**, 798–807 (2016).
4. F. Balzarotti et al., "Nanometer resolution imaging and tracking of fluorescent molecules with minimal photon fluxes," *Science* **355**, 606–612 (2017).
5. X. Liu et al., "Fluorescent nanowire ring illumination for wide-field far-field subdiffraction imaging," *Phys. Rev. Lett.* **118**, 076101 (2017).
6. G. Zheng, R. Horstmeyer, and C. Yang, "Wide-field, high-resolution Fourier ptychographic microscopy," *Nat. Photonics* **7**, 739–745 (2013).
7. J. Liang, Ed., *Coded Optical Imaging*, Springer International Publishing, Cham (2024).
8. M. Tang et al., "High-refractive-index chip with periodically fine-tuning gratings for tunable virtual-wavevector spatial frequency shift universal super-resolution imaging," *Adv. Sci.* **9**, 2103835 (2022).
9. E. G. Van Putten et al., "Scattering lens resolves sub-100 nm structures with visible light," *Phys. Rev. Lett.* **106**, 193905 (2011).
10. Ø. I. Helle et al., "Structured illumination microscopy using a photonic chip," *Nat. Photonics* **14**, 431–438 (2020).
11. H. Yilmaz et al., "Speckle correlation resolution enhancement of wide-field fluorescence imaging," *Optica* **2**, 424 (2015).
12. Y. Blau et al., "Double moiré structured illumination microscopy with high-index materials," *Opt. Lett.* **41**, 3455 (2016).
13. I. I. Smolyaninov et al., "Far-field optical microscopy with a nanometer-scale resolution based on the in-plane image magnification by surface plasmon polaritons," *Phys. Rev. Lett.* **94**, 057401 (2005).
14. I. I. Smolyaninov et al., "Super-resolution optical microscopy based on photonic crystal materials," *Phys. Rev. B* **72**, 085442 (2005).
15. A. Ono, J. Kato, and S. Kawata, "Subwavelength optical imaging through a metallic nanorod array," *Phys. Rev. Lett.* **95**, 267407 (2005).
16. F. Wei and Z. Liu, "Plasmonic structured illumination microscopy," *Nano Lett.* **10**, 2531–2536 (2010).
17. A. Bezryadina et al., "Localized plasmonic structured illumination microscopy with gaps in spatial frequencies," *Opt. Lett.* **44**, 2915 (2019).
18. Y. U. Lee et al., "Ultrathin layered hyperbolic metamaterial-assisted illumination nanoscopy," *Nano Lett.* **22**, 5916–5921 (2022).
19. Y. U. Lee et al., "Organic hyperbolic material assisted illumination nanoscopy," *Adv. Sci.* **8**, 2102230 (2021).

20. K. N. Fish, "Total internal reflection fluorescence (TIRF) microscopy," *Curr. Protoc. Cytom.* **50**(1), 12.18.1–12.18.13 (2009).
21. Q. Liu et al., "Total internal reflection fluorescence pattern-illuminated Fourier ptychographic microscopy," *Opt. Lasers Eng.* **123**, 45–52 (2019).
22. H. J. Lezec, J. A. Dionne, and H. A. Atwater, "Negative refraction at visible frequencies," *Science* **316**, 430–432 (2007).
23. X. T. Geng et al., "Frequency comb transferred by surface plasmon resonance," *Nat. Commun.* **7**, 10685 (2016).
24. C. T. DeVault et al., "Suppression of near-field coupling in plasmonic antennas on epsilon-near-zero substrates," *Optica* **5**, 1557 (2018).
25. J. Zheng et al., "Active control of excitonic strong coupling and electroluminescence in electrically driven plasmonic nanocavities," *Sci. Adv.* **11**, eadt9808 (2025).
26. S. Cao et al., "Numerical analysis of wide-field optical imaging with a sub-20 nm resolution based on a meta-sandwich structure," *Sci. Rep.* **7**, 1328 (2017).
27. Y. Takakura, "Optical resonance in a narrow slit in a thick metallic screen," *Phys. Rev. Lett.* **86**, 5601–5603 (2001).
28. P. Yeh, *Optical Waves in Layered Media*, Wiley, New York (1988).
29. N. Jayakumar et al., "Chip-based label-free incoherent super-resolution optical microscopy," *Light Sci. Appl.* **14**, 259 (2025).
30. X. Yang et al., "High-throughput super-resolution imaging chip based on miniaturized full- frequency encoded-illumination," arXiv:2507.16693 (2025).
31. M. Lei et al., "Deep learning assisted plasmonic dark-field microscopy for super-resolution label-free imaging," *Nano Lett.* **24**, 15724–15730 (2024).
32. Q. Wu et al., "Localized plasmonic structured illumination microscopy using hybrid inverse design," *Nano Lett.* **24**, 11581–11589 (2024).
33. T. Chang, G. Adamo, and N. I. Zheludev, "Super-resolution imaging of limited-size objects," *Nat. Photonics* **20**, 421–427 (2026).

Haonan Zhang received his bachelor's degree from Harbin Institute of Technology. He is currently working toward a PhD degree in optical engineering at the College of Optical Science and Engineering, Zhejiang University. His research focuses on spatial-frequency-shift super-resolution imaging.

Xu Liu is currently a professor at the College of Optical Science and Engineering, Zhejiang University. He is a fellow of the Chinese Optical Society, Optica, and SPIE. His research focuses on super-resolution optical microscopy, optical thin films, and precision metrology and imaging for extreme optical conditions.

Qing Yang received her PhD from the College of Materials Science and Engineering, Zhejiang University, in 2006. She is currently a professor at the College of Optical Science and Engineering, Zhejiang University. Her research focuses on super-resolution imaging, high-resolution endoscope, and nanophotonics.

Biographies of the other authors are not available.